

This is a repository copy of *Geological evidence of an unreported historical Chilean tsunami reveals more frequent inundation*.

White Rose Research Online URL for this paper:

<https://eprints.whiterose.ac.uk/181878/>

Version: Published Version

---

**Article:**

Hocking, Emma, Garrett, Ed, Aedo, Diego et al. (2 more authors) (2021) Geological evidence of an unreported historical Chilean tsunami reveals more frequent inundation. Nature Communications Earth and Environment. 245. pp. 1-10. ISSN 2662-4435

<https://doi.org/10.1038/s43247-021-00319-z>

---

**Reuse**

This article is distributed under the terms of the Creative Commons Attribution (CC BY) licence. This licence allows you to distribute, remix, tweak, and build upon the work, even commercially, as long as you credit the authors for the original work. More information and the full terms of the licence here:

<https://creativecommons.org/licenses/>

**Takedown**


If you consider content in White Rose Research Online to be in breach of UK law, please notify us by emailing [eprints@whiterose.ac.uk](mailto:eprints@whiterose.ac.uk) including the URL of the record and the reason for the withdrawal request.

## Geological evidence of an unreported historical Chilean tsunami reveals more frequent inundation

Emma P. Hocking<sup>1</sup>, Ed Garrett<sup>2</sup>, Diego Aedo<sup>3</sup>, Matías Carvajal<sup>4</sup> & Daniel Melnick<sup>5</sup>

Assessing tsunami hazards commonly relies on historical accounts of past inundations, but such chronicles may be biased by temporal gaps due to historical circumstances. As a possible example, the lack of reports of tsunami inundation from the 1737 south-central Chile earthquake has been attributed to either civil unrest or a small tsunami due to deep fault slip below land. Here we conduct sedimentological and diatom analyses of tidal marsh sediments within the 1737 rupture area and find evidence for a locally-sourced tsunami consistent in age with this event. The evidence is a laterally-extensive sand sheet coincident with abrupt, decimetric subsidence. Coupled dislocation-tsunami models place the causative fault slip mostly offshore rather than below land. Whether associated or not with the 1737 earthquake, our findings reduce the average recurrence interval of tsunami inundation derived from historical records alone, highlighting the importance of combining geological and historical records in tsunami hazard assessment.

<sup>1</sup>Department of Geography and Environmental Sciences, Northumbria University, Newcastle-upon-Tyne, UK. <sup>2</sup>Department of Environment and Geography, University of York, York, UK. <sup>3</sup>Facultad de Ciencias Químicas, Universidad de Concepción, Concepción, Chile. <sup>4</sup>Instituto de Geografía, Pontificia Universidad Católica de Valparaíso, Valparaíso, Chile. <sup>5</sup>Instituto de Ciencias de la Tierra, TAQUACH, Universidad Austral de Chile, Valdivia, Chile.

email: [emma.hocking@northumbria.ac.uk](mailto:emma.hocking@northumbria.ac.uk)

Inadequate anticipation of the magnitude of great earthquakes in Sumatra (2004), Chile (2010) and Japan (2011) stemmed from over-reliance on short historical records that failed to account for variability in earthquake size, rupture style, tsunamigenesis and the existence of supercycles<sup>1–3</sup>. Moreover, even where long written histories exist, individual events may be missing due to failures in reporting<sup>4</sup> or loss of documents in times of instability or crisis (e.g. late fourteenth/sixteenth century Japan)<sup>5,6</sup>, or there may be periods where only low-quality records exist containing errors<sup>5</sup>. Although with other limitations, geological records are free from these problems, and it is therefore imperative that we supplement historical data with geologic records, in order to obtain robust long-term patterns to inform seismic and tsunami hazard assessments.

We show that this is the case for the area affected by the 1960 Chile earthquake (magnitude 9.5), in the 1000-km-long southernmost portion of the subduction zone formed between the Nazca and South America plates (Fig. 1). Besides the 1960 earthquake and other lesser events, this area experienced three great earthquakes in the historical past (since the mid-sixteenth century): in 1575, 1737, and 1837. Historical and geological evidence in the form of tsunami deposits in coastal environments<sup>7–12</sup>, and shaking-induced turbidites in lakes<sup>13,14</sup> and fjords<sup>15</sup>, suggest that the 1575 earthquake was similar in size and extent to that in 1960, and that both were much larger than those in 1737 and 1837. The combined evidence also suggests that large tsunamis accompanied the 1575, 1837 and 1960 earthquakes but did not in 1737. To explain the complete absence of tsunami

reports in 1737 and the along-strike distribution of building damage, Cisternas et al.<sup>16</sup> proposed a deep interplate rupture limited to the northern half of the 1960 rupture area, and restricted to beneath land, with limited capacity for tsunami generation. However, the lack of chronicles of a tsunami could also be attributed to uprisings that had driven settlers from most of the colonial outposts in the area<sup>9,16</sup>.

Given the limited eyewitness reports for pre-1960 south Chilean earthquakes and tsunamis, their hypothesised rupture areas and proposed mechanisms require testing with geological evidence from coastal sites. Between the long palaeoseismic records from Tirúa<sup>7,8,17,18</sup> (38.3°S) and Maullín<sup>9</sup> (41.6°S), spatially there is a gap in coastal geological evidence (Fig. 1), in which the effects of pre-1960 events are unknown. This paper addresses this gap by presenting diatom and sedimentological evidence for historical seismic events from a tidal marsh at Chaihuín, near Valdivia, close to the region of maximum 1960 slip. We aim to (1) identify and determine the timing of multiple earthquake and tsunami events from the sedimentary record; (2) use a diatom transfer function to quantify vertical coseismic deformation; and (3) test hypotheses for pre-1960 rupture areas derived from limited historical and geological records.

Tidal observations before and after the 1960 earthquake suggest  $0.7 \pm 0.4$  m of coseismic subsidence occurred at Chaihuín (39.95°S, 73.58°W; Fig. 2) in this event<sup>19</sup>, and sedimentological investigations confirm subsidence<sup>20</sup>. With respect to pre-1960 earthquakes, to date, the closest sites to Chaihuín providing geological evidence for the 1575 earthquake are ~180 km to the

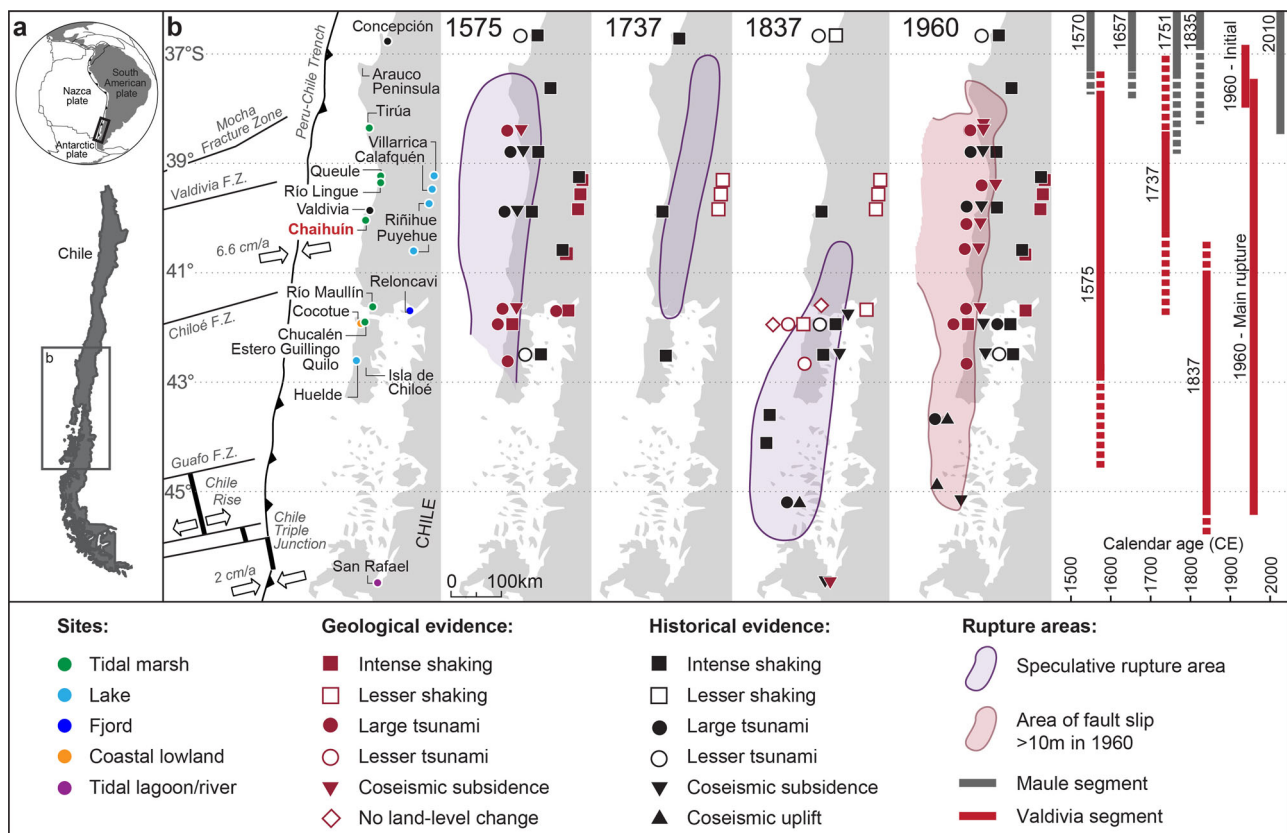


**Fig. 1** Geographical context of the study location and evidence of historical earthquakes in south-central Chile. Location of study area **a** within the regional tectonic setting and **b** within south-central Chile relative to sites referred to in the text and relative to rupture zones of the largest historical earthquakes. Geological evidence comes from Cisternas et al.<sup>9,10,16</sup>, Dura et al.<sup>7</sup>, Garrett et al.<sup>11</sup>, Hocking et al.<sup>20</sup>, Kempf et al.<sup>12</sup>, Moernaut et al.<sup>13,14</sup> and St-Onge et al.<sup>15</sup>; historical evidence from Cisternas et al.<sup>9,16</sup>. Rupture lengths of historic earthquakes compiled from Cisternas et al.<sup>16</sup>, Dura et al.<sup>7</sup> and Melnick et al.<sup>54</sup> (dashed lines indicate where rupture extents are uncertain). Plate motions from Angermann et al.<sup>55</sup>. Rupture zone maps adapted from original figure drawn by Marco Cisternas.



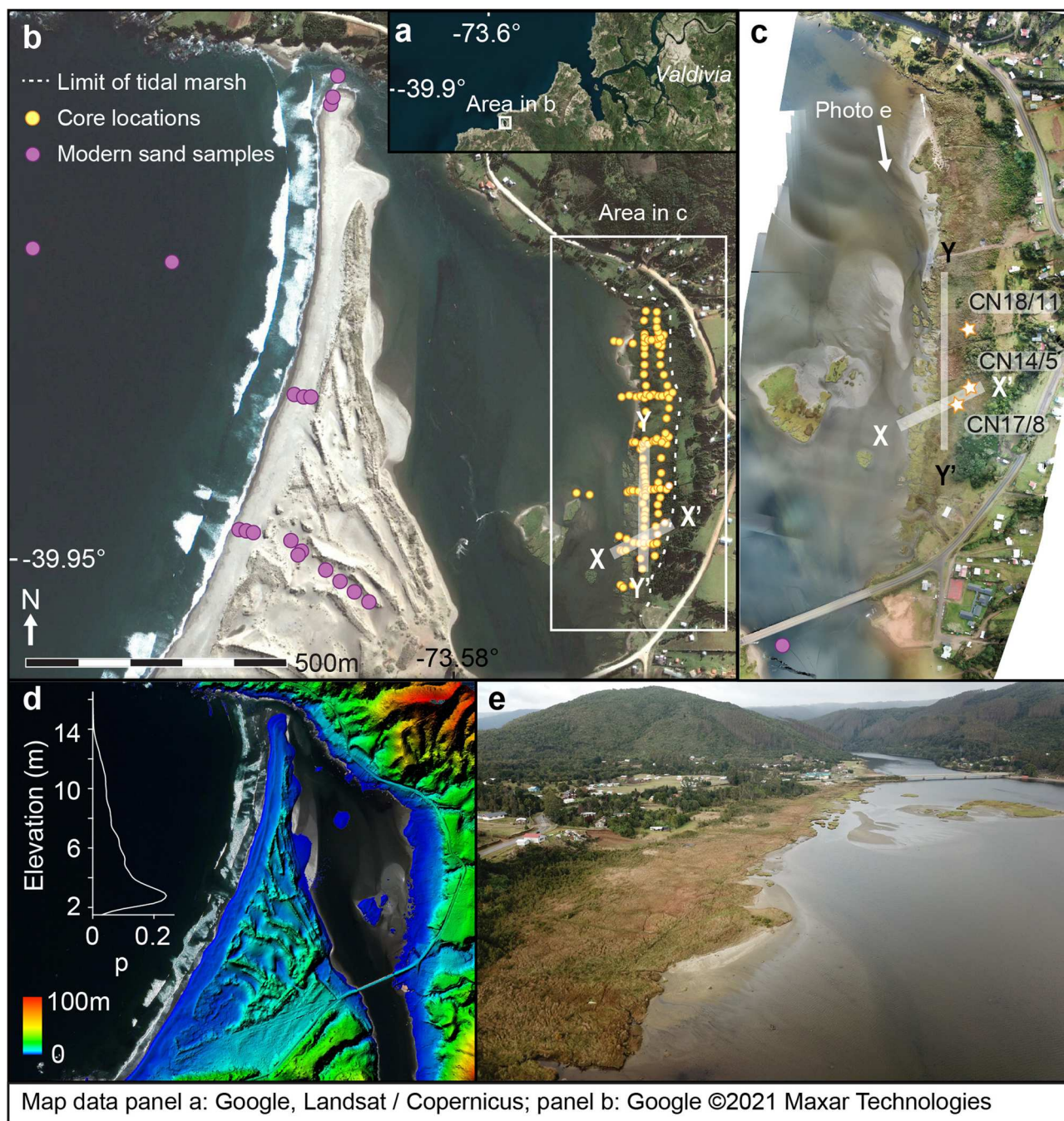


**Fig. 2** Location of tidal marsh and coring sites at Chaihuín. The study site is situated ~20 km southwest of Valdivia (a), occupying a sheltered embayment behind a large sand spit (~2 km long, ~500 m at its widest), which provides shelter from the Pacific Ocean that has promoted the development of tidal marshes and the accumulation of fine-grained sediments behind (b). The elevation distribution of the spit is extracted from the 1 m LiDAR Digital Terrain Model (d). The tidal range is low (mean higher high water [MHHW] = 0.526 m above mean sea level) and the marsh is close to the sea (<1.5 km), meaning modern diatoms should respond to tidal flooding. The sheltered location also increases the potential for preservation of evidence of seismic land-level changes and tsunami inundation. Coring locations shown on b, c—all cores (yellow dots) are presented in Aedo et al.<sup>22</sup>, transects X-X' and Y-Y' are presented in Fig. 3 and locations of cores analysed for diatoms marked by stars. Image sources: a Google, Landsat/Copernicus; b Google ©2021 Maxar Technologies; c, e orthomosaic and oblique drone images, authors' own; d LiDAR data from Forestal Arauco.

north (Tirúa<sup>7,8,17,18</sup>) and south (Río Maullín<sup>9</sup>), while the 1737 and 1837 events are not recorded anywhere in tidal marsh stratigraphy<sup>9,11</sup>, and their preservation in the geological record is limited to the south-central Chilean Lake District (39–40°S)<sup>14</sup> and coastal lowlands on Chiloé<sup>10</sup>. Chaihuín lies within the proposed rupture zone of the 1575 earthquake and tens of kilometres north

of the proposed 1837 rupture area (Fig. 1). If the 1737 earthquake ruptured the northern half of the 1960 rupture area<sup>16</sup>, Chaihuín occupies a key location for searching for its geological signature and for delimiting the northernmost extent of the 1837 rupture. Here we present geological evidence for a previously unreported tsunami in south-central Chile, which critically reduces the

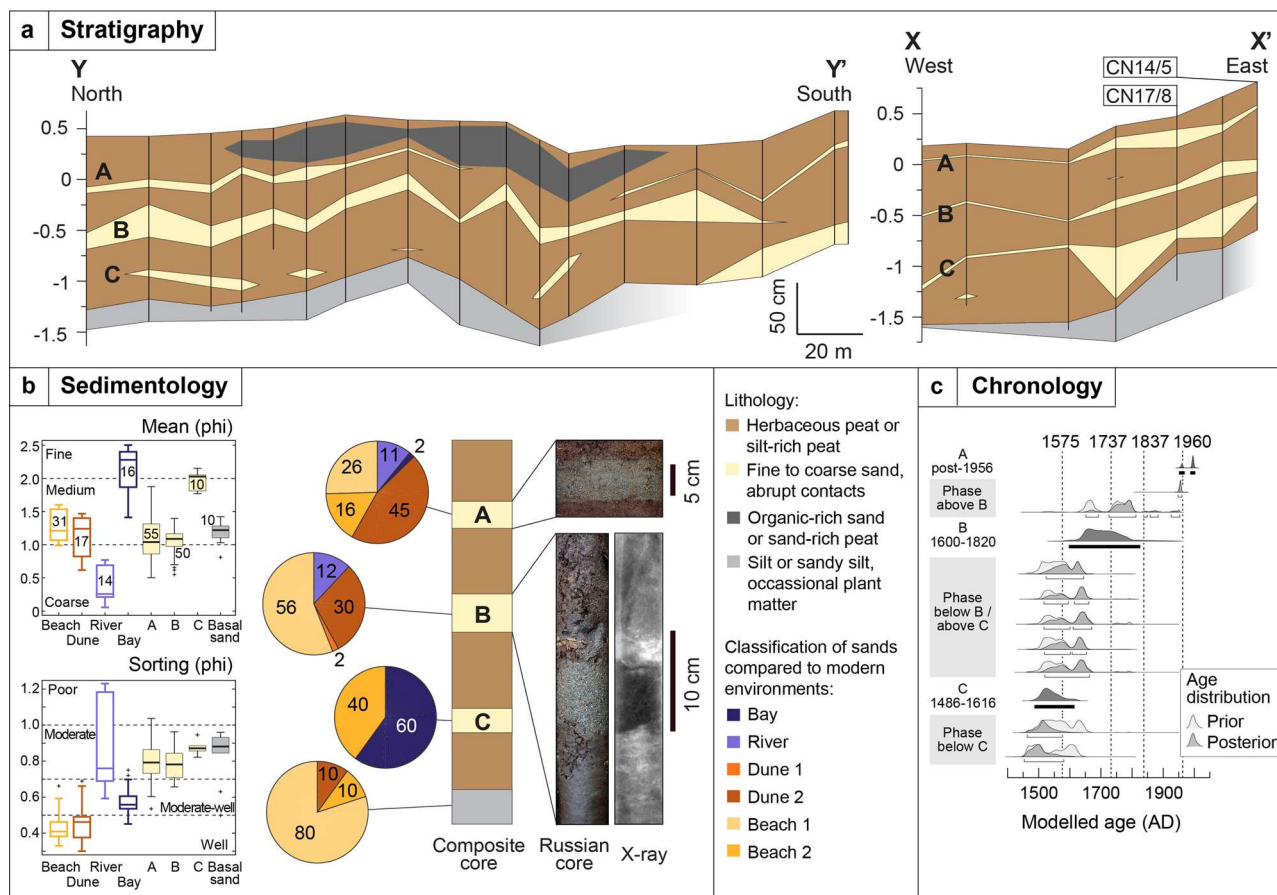


**Fig. 3 Geological evidence from Chaihuín.** **a** Stratigraphy of selected coring transects showing three laterally extensive sand sheets. Transect locations X-X' and Y-Y' shown on Fig. 2; **b** sedimentology of sand sheets, including grain size, sorting and clastic composition (%) classified relative to six modern environments established by discriminant analysis (see Supplementary Discussion), with images of sands A and B in CN17/8. Box-and-whisker plots show the statistical parameters measured in sand samples with the horizontal line inside the box representing the median, the box representing the upper and lower quartiles, the whiskers representing the minimum and maximum values excluding any outliers and the crosses the extreme outlier values. The number within each box indicates the number of samples in each group; **c** probability density functions (95.4%) of radiocarbon dates and modelled ages for the three earthquakes. Full radiocarbon results in Supplementary Table 1.

average recurrence interval of tsunami inundation derived from historical records alone.

## Results and discussion

**The Chaihuín stratigraphy.** Core transects (Fig. 2b) reveal three sand layers, intercalated between herbaceous peats, that are laterally extensive over 600 m across the marsh (Fig. 3a). In all cases, the sand layers have sharp lower contacts and transitional upper contacts. Ten accelerator mass spectrometric (AMS) radiocarbon dates modelled using a Bayesian phased sequence model provide the chronology (Fig. 3c and Supplementary Table 1). The age of plant macrofossils immediately beneath the upper layer, sand A, are consistent with burial by the 1960 tsunami. The age model places the deposition of the middle sand B at 1600–1820 and lower layer, sand C, at 1486–1616 CE. The calibrated age ranges for sands B and C are reasonably broad due to plateaux in the radiocarbon calibration curve, which affect dates from the seventeenth to twentieth centuries<sup>21</sup>.

The sedimentology and mineralogical signatures of the sand sheets are described in detail elsewhere based on over 100 hand-driven cores<sup>22</sup> and summarised in Supplementary Discussion; here we analyse diatoms in three representative cores and present reconstructions of marsh surface elevation change over time from a diatom-based transfer function (Fig. 4 and Supplementary

Data 1). From diatom analysis of the three cores, we identified 170 species indicative of differing tolerances to tidal inundation. Only 14 species were absent from a previously published modern training set that includes 29 samples from Chaihuín<sup>20</sup>, and 9 of these species constituted <1% of any one sample. *Fallacia ny* was the only species absent from the modern samples that constituted >2% of any sample (comprising 4–5% in 2 non-sand samples).

The laterally extensive uppermost coarse to medium-grained sand sheet (A) is mid grey, varies in thickness between 1 and 19 cm, has a median grain size of 0.49 mm and is upwards fining (0.27–0.71 mm) in 61 cores (80% of those in which A is preserved, massive in the others). The marsh grades steeply into freshwater scrub, and there is no sand unit in cores just above the high marsh limit. There is an abrupt contact between the sand and dark brown silty herbaceous peat below, which contains plant material including below-ground stems (rhizomes) of *Scirpus americanus*. In many cores, there are rip-up clasts (~2 cm) of peat encased in the sand sheet, as well as vegetation rooted in the peat below. The peat below the sand sheet contains a diatom assemblage that is almost entirely composed of species found on the contemporary high marsh above mean higher high water (MHHW) (e.g. *Eunotia praerupta*, *Nitzschia acidoclinata*), with higher elevation optima than the diatoms found in the herbaceous peat above the sand unit (e.g. *Rhopalodia constricta*) (Fig. 4a). The overlying peat also contains low, albeit important,



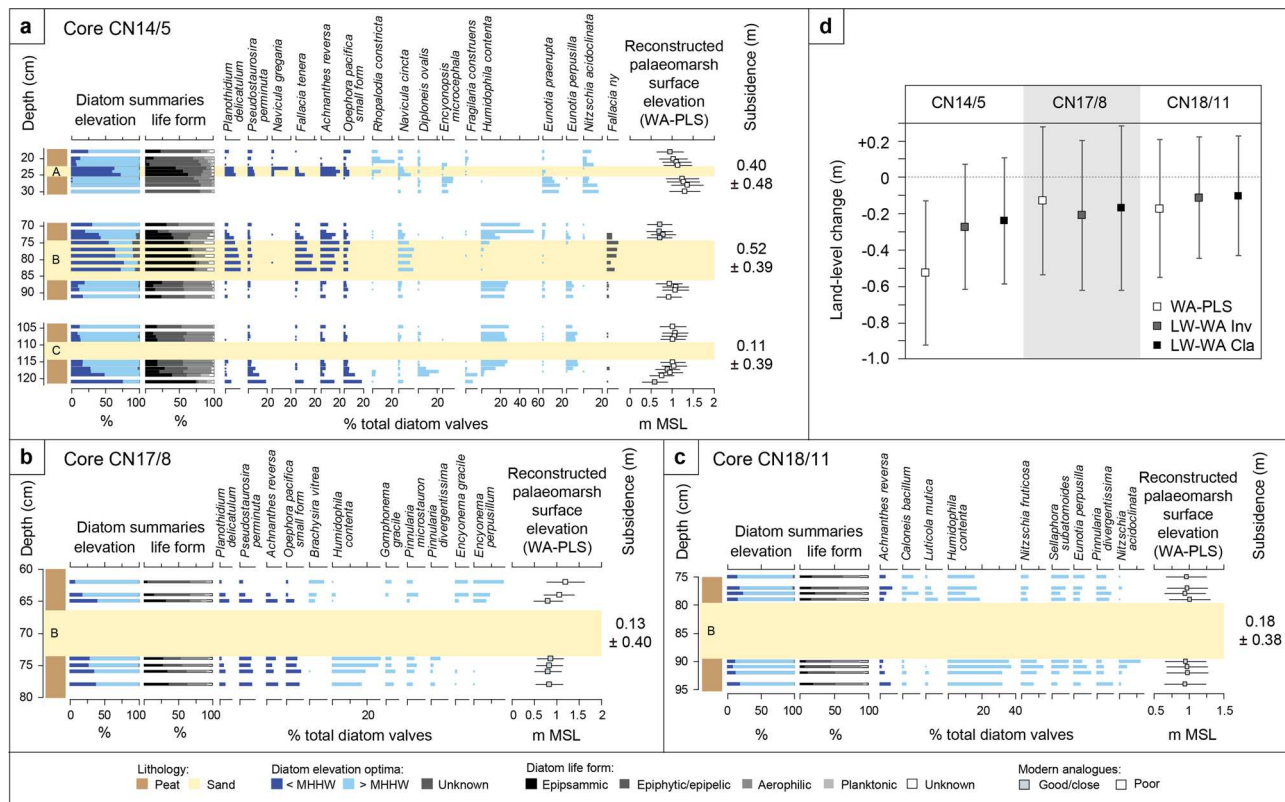


**Fig. 4** Diatom assemblages and estimates of land-level change derived from a regional south-central Chile transfer function for three cores from **Chaihuin**. **a–c** Diatom assemblage summaries and dominant taxa in cores CN14/5 (**a**), CN17/8 (**b**) and CN18/11 (**c**) at elevations of 0.88, 0.89 and 1.10 m above mean sea level (MSL), respectively. Elevation optima of diatom species are classified based on weighted averaging of the modern training set and reported relative to mean higher high water (MHHW). The modern analogue technique was used to calculate the squared chord distance to the closest modern analogue, and the threshold for a fossil sample having a close modern analogue is defined as the 20th percentile of the dissimilarity values (MinDC) for the modern training set<sup>44</sup>. Reconstructed palaeomorph surface elevations (PMSE) and coseismic subsidence are shown from the weighted averaging partial least squares (WA-PLS) model only. **d** Estimates of coseismic subsidence in 1737 from three cores and three different diatom-based transfer function approaches, showing 95.4% uncertainties.

percentages (5–24%) of taxa with elevation optima below MHHW. By contrast to the peats, sand A is dominated by species with lower elevation optima (59–72% of the total assemblage have optima below MHHW), including *Achnanthes reversa* and *Planorbulina mediterranensis*.

The middle brown-grey to dark grey mica-rich coarse to medium-grained sand sheet (B) is similarly laterally extensive across the entire marsh, varying in thickness between 2 and 32 cm. It has a median grain size of 0.47 mm and is upwards-fining (0.38–0.68 mm) in 31 cores (50% of those in which B is preserved, massive in others), but rip-up clasts of peat were only occasionally observed. In some cases, we observe a 2–4-cm-thick cap of horizontally bedded detrital plant fragments and wood at the top of the sand layer. The sand sheet abruptly overlays a red-brown to dark brown silty herbaceous peat with variable silt content and humification. *Humidophila contenta* dominates the diatom assemblage in the peat below sand B (up to 37% of the assemblage) and is also present in the peat overlying the sand sheet, which remains dominated by species with elevation optima above MHHW. In the core from the lowest contemporary marsh elevation (CN14/5, Fig. 4a), there is an increase in low marsh diatom species (elevation optima below MHHW) above the sand compared to below (e.g. *A. reversa*, *P. mediterranensis*). Diatom assemblages are relatively consistent across the five samples from the sand unit, with 54–76% of the assemblages being species with elevation optima below MHHW, including *A. reversa*, *Fallacia tenera* and *P. mediterranensis*.

A third sand deposit (C) is found in 16 cores at the southern end of the marsh, although still traceable over 200 m and across most cores that penetrated deep enough to potentially sample sand C. The deposit is a dark grey fine to medium-grained massive sand (median grain size 0.25 mm, range 0.22–0.29 mm), with a maximum thickness of 51 cm and contains occasional rip-up clasts from the buried organic unit below encased in the sand. The basal contact is abrupt, with the sand overlying a brown clayey silt with occasional herbaceous plant remains, humified organic matter and woody plant material. The organic horizon below sand C contains more diatom species typically found at lower elevations in the tidal frame than the peats below A and B (Fig. 4a). There is also a change in species composition approaching the top of the peat, with abundances of *Opephora pacifica* and *Pseudostatosira perminuta* decreasing and *H. contenta* and *E. perpusilla* increasing from the base to top of the peat below sand C. Also in contrast to the other two buried organic deposits, there is a change in species composition approaching the top of the peat and samples immediately above and below sand unit C have very similar diatom assemblages, dominated by *H. contenta* and *E. perpusilla*. Diatom preservation in the sand unit was very poor, and it was not possible to obtain representative counts from this unit.

Brown silty herbaceous peats separate the three sand sheets, deposited intertidally on the basis of their diatom composition. In addition to the relative variations in freshwater and brackish diatom composition of peats described above, the peat units also

vary in their degree of humification. While peats below sands A and C contain humified organic matter, the peat below sand B is unhumified. Additionally, two layers of highly humified black peat were observed immediately above and below sand A in low marsh cores from the southwest of the marsh, varying in thickness between 1 and 15 cm.

**Evidence for a locally sourced tsunami.** We interpret all three sand sheets as being deposited by locally sourced tsunamis, rather than far-field tsunamis or non-seismic processes (e.g. storms, river floods or aeolian processes). This is based primarily on coincident land deformation, and also upon their lateral extent, diatom composition, and sedimentological signatures. Dealing first with the latter lines of reasoning, sands A and B are not only dominated by marine sublittoral and epipsammic diatom species but also contain substantial numbers of benthic silty intertidal mudflat and freshwater taxa, which also dominate the underlying peats. This is consistent with mixed diatom assemblages in tsunami deposits worldwide and indicative of tsunamis eroding, transporting and redepositing diatoms from diverse environments as they cross coastal and inland areas<sup>23–26</sup>. The presence of marine and tidal flat diatoms excludes deposition of sand by river flooding<sup>25,27</sup>, and statistical comparison of the sedimentological and mineralogical signatures of the sands with modern depositional environments, reported by Aedo et al.<sup>22</sup> and summarised in Supplementary Discussion, further supports a seaward rather than fluvial sediment source. We observe a maximum sedimentary contribution of 12% from upstream fluvial sources (Fig. 3b) and do not observe erosional or depositional features characteristic of fluvial flood deposits, such as a high basal mud content reflective of suspended loads during the initial stages of flooding or inverse grading as energy increases<sup>28</sup>.

Meteorologically driven deposition of the sands, either during storm surges or other transient sea-level fluctuation events (e.g. El Niño), is discounted as the diatoms in the overlying organic units demonstrate lasting ecological change<sup>27,29</sup>. While a non-tsunamiogenic earthquake followed closely in time by a large storm surge may impact diatom assemblages in the same way, there are several further characteristics of the three sand sheets which are consistent with a tsunami origin, even though these, in themselves, are not diagnostic. These include the lateral extent (traceable across 230 m), upwards-fining grain size of sand sheets A and B, and clasts of underlying peats observed within sands A and C and occasionally within B. The absence of extreme climatic phenomena, such as hurricanes and tropical storms, in the Chaihuín area during the historic period also minimises the possibility of finding storm deposits. However, while it is recognised that the above criteria cannot be used individually to confirm tsunami deposition, it is the combination of all sedimentological and diatom evidence that we use here in support of the most compelling evidence for tsunami deposition, which comes from the accompanying abrupt land-level change. The latter rules out deposition by tsunamis sourced in the far-field, storms or aeolian processes.

**Evidence for coseismic land-level change.** Following established criteria<sup>30,31</sup>, we use the sedimentary and diatom evidence to propose that the Chaihuín sequence records three earthquake events, associated with vertical coseismic deformation and tsunami deposition. Diatom assemblages from immediately below sand layers A and B are characterised by species with higher elevation preferences than those found immediately above the sands, suggesting decreases in marsh surface elevation consistent with coseismic subsidence (Fig. 4). Diatom assemblages show minimal change across sand layer C; instead a transition occurs

prior to event C whereby species with lower elevation preferences are replaced by those with higher elevation preferences, indicating net emergence prior to event C followed by minimal coseismic subsidence.

The transfer function reconstructs  $0.35 \pm 0.42$  m of subsidence occurred in event A, which local testimony and radiocarbon dating confirm to be the 1960 earthquake. Compared to our previous estimate for this event<sup>20</sup>, refining the transfer function method and expanding the modern training set here, reduces the uncertainty by 0.26 m. Reconstructed subsidence agrees with observations of  $0.7 \pm 0.4$  m<sup>19</sup>. By contrast, the transfer function reconstructs very minor subsidence of  $0.10 \pm 0.36$  m occurred in event C, but this needs confirmation from analyses of additional cores.

The transfer function predicts that coseismic subsidence occurred in event B, with reconstructions varying between  $0.10 \pm 0.33$  and  $0.52 \pm 0.39$  m, and averaging  $0.22 \pm 0.38$  m (Fig. 4d). While this is close to the detection limit of coseismic land-level change<sup>30</sup> and the error term is large compared to the amount of deformation, we interpret event B as being associated with net submergence for two reasons. First, changes in diatom-inferred marsh elevations between pre- and post-earthquake samples are greater than other sample-to-sample changes. Second, all nine reconstructions, regardless of core location or transfer function approach, indicate submergence rather than a mixture of submergence and emergence (Fig. 4d).

**Linking the geologic and historical records.** Despite the broad modelled age ranges for events B and C of 1600–1820 and 1486–1616 CE, respectively, each range only includes one historically reported earthquake. If the historical catalogue is complete, sands B and C represent tsunamis accompanying the 1737 and 1575 earthquakes, respectively. Although other great tsunamiogenic earthquakes occurred in the time range of event B (1657, 1730, 1751), their rupture areas have been placed much further north<sup>8,32</sup> and therefore are very unlikely sources for the observed deformation. Age ranges do not include 1837; therefore, absence of evidence for this earthquake at Chaihuín supports the chronicle-based interpretation that the 1837 rupture area lies further south<sup>11,16</sup>. The preservation of turbidites from 1837 at sites to the north of Chaihuín<sup>14</sup> is consistent with observations of earthquake-triggered turbidites some distance outside the rupture zone, as observed for the  $M_w$  8.8 2010 Maule earthquake<sup>14</sup>.

**Implications for the rupture depth in 1737.** The Chaihuín record provides the first evidence for crustal deformation during the 1737 earthquake and the first evidence for the earthquake being tsunamiogenic. While the nearshore bathymetry and orientation of the coastline may amplify tsunami inundation and the abundant sediment source may enhance the potential for evidence creation during even moderate tsunamis, the direction of land-level change at Chaihuín (subsidence) calls for reconsideration of the associated rupture depth. While correlation with evidence of shaking-induced turbidites from Calafquén and Riñihue lakes<sup>14</sup>, along with the absence of a 1737 event in sedimentary records from Río Maullín and Chucalén to the south<sup>9,11</sup>, supports the hypothesis that a smaller section of the plate interface ruptured in 1737 (between 39 and 41°S) than in 1960 and 1575<sup>14</sup>, the Chaihuín record also forms an important constraint on the depth of local slip in 1737.

By combining deformation and tsunami modelling, we show that our evidence of coastal subsidence and tsunami inundation at Chaihuín is better explained by offshore, shallow megathrust slip rather than by deeper slip below land as previously suggested<sup>16</sup> (Fig. 5 and Supplementary Fig. 1). This is demonstrated by a

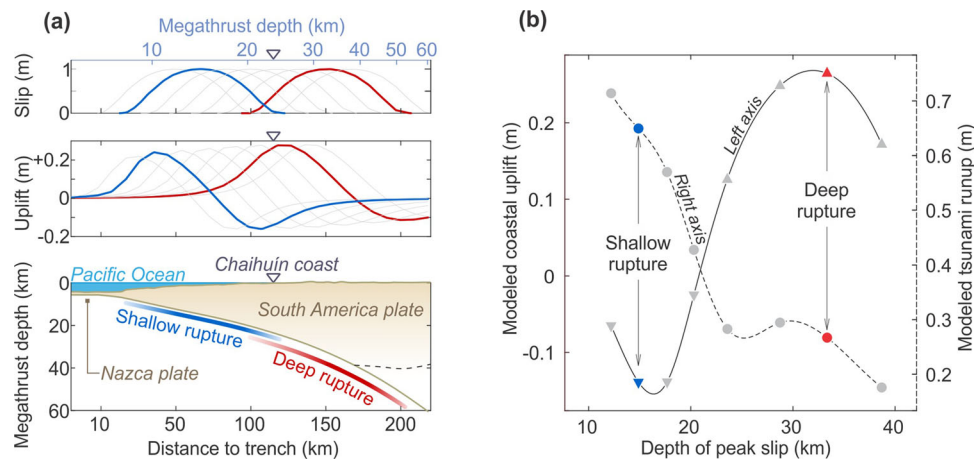


**Fig. 5 Results of model tests to show that the 1737 rupture must have been confined to the offshore region at shallower fault depths than previously proposed.** **a** The lower panel shows the trench-normal section of the megathrust and seafloor geometry at the latitude of Chaihuín used in the modelling experiment. The upper panel shows the bell-shaped slip distributions for a suite of eight earthquake ruptures and the middle panel shows the modelled vertical surface deformations using an elastic dislocation model (see “Methods”). The red and blue curves are the deep and shallow ruptures used as illustrative examples in the text. In this suite of models, the rupture width and peak slip are fixed at 100 km and 1 m, respectively, and the rupture location is systematically shifted horizontally in the trench-normal direction to represent ruptures at different depths. **b** Summary plot showing the modelled coastal uplift (left vertical axis) and tsunami runup (right vertical axis) predicted by the suite of models. Note that coastal subsidence can only be produced by offshore ruptures, with slip shallower than ~20 km. Ruptures deeper than this produce uplift at the coast. This opposing pattern of coastal deformation between shallow versus deeper ruptures is insensitive to how much slip is prescribed at the fault. Supplementary Fig. 1 shows the results for two different suite of models, in which the rupture width varies by fixing the updip (Supplementary Fig. 1a) and downdip (Supplementary Fig. 1b) limits.

simple numerical experiment designed to find the most likely depth range of the causative earthquake rupture that can explain the coastal subsidence inferred at Chaihuín and also the tsunami inundation.

Our numerical approach (see also “Methods”) leverages the sensitivity of the deformation sign (uplift or subsidence) and tsunami size at the Chaihuín coast to the depth of megathrust slip<sup>33</sup> (Fig. 5). An earthquake rupture with maximum slip at 33 km fault depth (Fig. 5a, red model), as previously inferred from historical records<sup>16</sup>, will result in coastal uplift and a relatively small tsunami. Instead, if the rupture occurs offshore (Fig. 5a, blue model), the deformation will result in coastal subsidence and a much larger tsunami. From a systematic analysis in which the hypothetical rupture models are shifted horizontally in the trench-normal direction or vertically in the depth direction (Fig. 5a, upper panel), we conclude that subsidence at the Chaihuín coast could only be produced by ruptures placed mainly offshore, at average megathrust depths shallower than 20 km (Fig. 5b, downward triangles). Deeper ruptures will produce coastal uplift and consequent smaller tsunamis (Fig. 5b). The same conclusion is reached by varying the rupture width with fixed updip and downdip limits (Supplementary Fig. 1).

Our conclusions are independent of the use of a normalised unit displacement in all models (i.e. 1 m at the centre of its corresponding bell-shaped rupture) because the opposing effects of deep versus shallow ruptures at Chaihuín are insensitive to the magnitude of slip involved and depend on its locus. The amount of slip determines the magnitude of deformation but not its sign due to the elastic response of the crust during earthquakes<sup>34</sup>. However, with evidence at only one location we only feel confident to constrain the depth range but not the magnitude nor along-strike extent of the causative slip. Therefore, from our numerical experiment we conclude that to produce subsidence at the Chaihuín coast, an offshore rupture likely shallower than 20 km is required as a deeper source would result in coastal uplift. This is also consistent with the inferred tsunami heights (Fig. 5b), which are larger for a shallower rupture and therefore more likely

to produce inundation on land independent of the local topography. This geologically-based inference of an offshore rupture (blue curve in Fig. 5b) contrasts with the deeper rupture below land in Fig. 5b) previously inferred from historical observations alone<sup>16</sup>.

**Implications for tsunami recurrence intervals.** The average interval between the three events preserved at Chaihuín, 193 years, is shorter than the interval proposed for full segment 1960-style ruptures of 270–280 years<sup>9,11,14</sup>. This supports the notion that the Chilean subduction zone displays a variable rupture mode, in which the size, depth, tsunamigenic potential and recurrence interval vary between earthquakes<sup>10</sup>. Of greatest importance, however, is the shorter average recurrence interval of tsunami inundation than previously reported. With the addition of the 1737 tsunami alongside previously known events in 1960, 1837 and 1575, the historical recurrence interval for tsunamis generated anywhere along the Valdivia segment of the Chilean subduction zone is reduced to 130 years. This holds even if the inferred tsunami inundation is not associated with the 1737 earthquake, but with another earthquake of similar age missed in the historical catalogue.

## Conclusions

Locally sourced tsunami deposition is the favoured mechanism for the emplacement of three sand sheets at Chaihuín tidal marsh, south-central Chile. We infer this mechanism based on the lateral extent of the deposits, sedimentological composition compared to modern environments, characteristic sedimentary structures including rip-up clasts, marine diatom assemblages that exclude a fluvial source, and most importantly, coincident abrupt marsh submergence that excludes storm surge deposition.

Tidal marsh stratigraphy and changing diatom assemblages record three episodes of abrupt land-level change accompanying the tsunami deposits. Modelled ages for the youngest and oldest deposits correspond with known tsunamigenic earthquakes in 1960 and 1575 CE. The intervening event is consistent in age with



the 1737 earthquake, for which no tsunami has previously been reported. The lack of evidence for land-level change or tsunami inundation consistent with a historically documented earthquake and tsunami in 1837 confirms Chaihuín lies to the north of the 1837 rupture area.

Our identification of the first evidence for a tsunami accompanying the 1737 earthquake reveals tsunami inundation has occurred more frequently than previously thought along the Valdivia segment of the Chilean subduction zone. Furthermore, by using coupled deformation–tsunami modelling, guided by the new geological evidence, we show that the 1737 earthquake ruptured mainly offshore, at fault depths much shallower than previously proposed from historical records alone. These results provide further support for the spatiotemporal variability in ruptures within a supercycle between the 1575 and 1960  $M_w > 9$  earthquakes.

This study highlights that historical records may not provide complete documentation of the occurrence and characteristics of earthquakes and tsunamis occurring during the historical period. Geological evidence is essential for not only extending earthquake and tsunami histories into the past, but for verifying and supplementing historical records. This has global significance anywhere where there could be issues of absent or incomplete reporting of events, or loss of records, particularly in times of local or national crisis.

## Methods

Tidal marsh sediments are excellent recorders of relative sea-level changes<sup>35</sup>, and in regions of palaeoseismicity, sequences of organic soils interbedded with minerogenic units often reflect vertical land-level changes that occur both coseismically during megathrust earthquakes and through intervening interseismic periods<sup>36,37</sup>. Diatoms, siliceous microfossils incorporated within these tidal marsh sediments, are used to quantify vertical land-level changes associated with great earthquakes due to the close control of salinity on their distribution in intertidal environments, as well as their high preservation potential in coastal sediments<sup>38</sup>. Due to their robust valves, diatoms are also widely used to determine the provenance of tsunami sediments and changing flow conditions during tsunamis<sup>23,38–40</sup>. In this way, diatoms have been used to reconstruct the history of earthquakes and tsunami worldwide over multi-millennial timescales<sup>25,31,36–38</sup>, providing long-term perspectives on the recurrence, magnitude and variability of earthquakes occurring along subduction zones.

**Lithostratigraphy.** We used marsh front exposures and 130 hand-driven gouge and Russian cores (collected between 2013 and 2018) to reveal the stratigraphy. We sought evidence for tsunami inundation in the stratigraphic record, but as sand sheets can be deposited by both seismic and a range of non-seismic sedimentary, fluvial, oceanographic or atmospheric processes, particularly storm surges<sup>29,31</sup>, we employed transects of cores (Fig. 2b) to assess the lateral extent and continuity of sand sheets. We interpret sand sheets as being of seismic origin where these abruptly overlay organic peats in cores correlated over 10s to 100s of metres, with diatom, chronological and sedimentological analyses providing further lines of evidence<sup>30,31</sup>.

**Sedimentological and mineralogical analyses.** Methods used to characterise the sediments according to grain size and mineralogy are detailed in Aedo et al.<sup>22</sup>. To summarise briefly here, 25 subsamples (50–140 cm<sup>3</sup>) were taken from the sand sheets recovered from cores to analyse the granulometry and mineralogy. Granulometric analysis followed the particle settling velocity method<sup>41</sup>, and central tendency and mean dispersion were calculated using GRANPLOT<sup>42</sup>. The mineral composition was estimated based on a modal count with a binocular microscope of 200 grains. In order to establish the origin of the sands, core sand samples were statistically compared to 22 samples taken from a series of modern environments (beach, sand bar, dunes, estuary and the outer bay, Fig. 2b). Discriminant analysis was performed using the modern samples and four granulometric parameters (mean, selection, skewness, normalised kurtosis) as predictor variables, using the Statgraphics Centurion XVI software version 16.2.04. Finally, we also scanned selected core sections using a Geotek X-ray core imaging system at Durham University. The scanner operated at 125 kV and we used Fiji<sup>43</sup> to visualise the data.

**Diatom analysis.** A key criteria in assessment of tsunami versus non-seismic sources of sand sheets is coincident vertical land-level change<sup>30,31</sup>. We therefore analysed fossil cores for diatoms due to their well-documented utility in relative sea-level reconstruction, which is based on the relationship between species and

elevation<sup>35</sup>. Due to varying tolerances to salinity, the frequency and duration of tidal inundation and sediment type, diatom assemblages show distinct vertical zonation across a tidal marsh. We discuss these contemporary relationships between species and marsh surface elevation in Hocking et al.<sup>20</sup> and use the modelled contemporary relationships to quantitatively relate the changes seen in fossil diatom assemblages to past changes in the elevation of the marsh surface via a transfer function. We prepared samples for diatom analysis following standard methods<sup>40</sup> and counted a minimum of 250 diatom valves per sample.

In the transfer function, we use a regional south-central Chile modern diatom training set (Supplementary Data 1), updated from Hocking et al.<sup>20</sup>. The training set consists of 148 modern samples from 6 marshes in south-central Chile (Queule, Río Lingue, Isla del Rey/Valdivia, Chaihuín, Quilo and Estero Guilingo; Fig. 1). We use a regional modern training set due to the superiority of the regional south-central Chile model over sub-regional and local models, both in terms of agreement with observations in 1960 and in providing fossil samples with the closest modern analogues<sup>20</sup>. This also follows studies elsewhere that favour regional models, particularly as the difference in age between modern and fossil samples increases and the present day marsh may no longer capture the full environmental conditions potentially present in older records<sup>44–46</sup>. While modern sample sites span ~280 km, the training set does include 29 local samples from Chaihuín, as previous studies have also highlighted the importance of including samples from the local area where possible<sup>20,44</sup>. Since publication of the modern training set in 2017, we have collected further tidal data to improve the tidal modelling and calculation of modern sample elevations, as well as updated nomenclature. These changes have resulted in a minor change in transfer function performance and required that modern tidal flat samples and those from elevations above a standardised water level index (SWLI) of 350 be excluded from the training set (see Hocking et al.<sup>20</sup> for explanation of standardisation of sample elevations to account for tidal range differences between sample sites). Outside of this threshold range, the transfer function does not do well at predicting elevation. The updated modern training set contains 7 samples that were not included in 2017 and excludes a further 33 samples, which were previously included.

Development of the transfer function and evaluation of transfer function performance builds upon Hocking et al.<sup>20</sup>. We follow the same approach of using weighted-averaging partial least squares (WA-PLS) regression (due to the unimodal nature of the diatom data) with bootstrapping cross-validation (1000 cycles), and assessed performance by using the Modern Analogue Technique to calculate the similarity between modern and fossil assemblages (reported as minimum dissimilarity coefficients). We also run a locally weighted-averaging (LW-WA) transfer function model, with cross-validation and both classical and inverse deshrinking, in order to compare reconstructions derived by different transfer function methods. The three models used in the transfer function—WA-PLS (component 2), LW-WA (classical deshrinking) and LW-WA (inverse deshrinking)—have  $r^2_{\text{boot}}$  values between observed and predicted elevations of 0.72, 0.79 and 0.79, respectively, and root mean square error of prediction of 25.72, 22.78 and 23.42 SWLI units, respectively (equating to 0.12–0.14 m at Chaihuín).

The output of the transfer function is the palaeomorph surface elevation (PMSE) associated with each fossil sample. To quantify coseismic deformation, we subtract the reconstructed pre-earthquake PMSE from the post-earthquake PMSE and correct for sediment accumulation, including tsunami deposition. The associated 95.4% ( $2\sigma$ ) uncertainty term is the square root of the sum of the squared sample-specific standard errors for pre- and post-earthquake samples. In order to give an overall estimate of deformation for each earthquake, we average transfer function outputs from all cores and model approaches, rather than relying on a single method.

**Chronology.** We assigned ages to sand layers by using AMS radiocarbon dating of herbaceous plant macrofossils found immediately above and below the sands. We selected above ground parts of terrestrial plants that were horizontally bedded within the sediment matrix wherever possible. Samples were analysed at high precision using multiple graphite targets, due to the potential problems for radiocarbon dating and calibrating ages from the past 400 years associated with plateaux in the radiocarbon curve<sup>21,47</sup>. We calibrated dates using the SHCal20 calibration curve<sup>48</sup> or the post-bomb atmospheric southern hemisphere calibration curve<sup>49</sup> for the samples exceeding 100% modern carbon. We report  $2\sigma$  age ranges in years CE. We used a Bayesian phased sequence model within OxCal (version 4.4) to refine the calibration solutions; this constrains the relative order and grouping of events<sup>50</sup>. The model includes 10 macrofossil ages; one charcoal sample was excluded due to the anomalous old age, which was out of stratigraphic order (Supplementary Table 1).

**Rupture and tsunami modelling.** We modelled coastal deformation at Chaihuín due to megathrust slip using a three-dimensional (3D) dislocation model in a uniform elastic half-space with an assumed Poisson's ratio of 0.25. We used an extensively benchmarked computer code<sup>51</sup> that numerically integrates the point-source dislocation solution (Green's function)<sup>34</sup> over a 3D megathrust and yields displacement values on the surface of the model. Given that we are interested in constraining the location of the rupture in the dip direction rather than in the strike direction, we constructed a megathrust that is uniform along strike and long enough to avoid 3D or edge effects. The megathrust geometry was constructed by

discretizing slab data<sup>52</sup> at the latitude of Chaihuín into small triangular fault elements, each representing individual point-sources. Deformation at the surface was computed by the sum of the contributions from all the triangular sources. All tested earthquake rupture models consider a bell-shaped slip distribution in the dip direction with a peak slip of 1 m at its centre, which tapers updip and downdip<sup>51</sup>. The peak slip is fixed at unity because the sign of coastal deformation (either subsidence or uplift) depends only on the rupture depth. Constraining the slip magnitude or how it varied along-strike would require additional evidence at other sites along the south-central Chile coast. All models assume that the direction of coseismic slip (rake) is roughly 90° to represent pure dip-slip faulting.

All tsunami simulations were computed by using a finite-difference method on the actual bathymetry offshore Chaihuín. We used the well-validated numerical model COMCOT, which solves the linear shallow water equation (LSWE) and nonlinear shallow water equation using a leap-frog scheme on a staggered and nested grid system<sup>53</sup>. We assumed the initial sea-surface elevation to be equal to the vertical seafloor deformation due to earthquake faulting of each rupture model. The two-dimensional bathymetric profile, which we uniformly extended along strike, was constructed from global gridded bathymetric data ([www.gebco.net](http://www.gebco.net)), from which a two-level nested grid system was used. The first grid level with ~500 m spatial resolution was used in the source region and in deep water, where the LSWE were considered. In the coastal area of Chaihuín, we upsampled the GEBCO data by a factor of 5 to obtain a finer grid of ~100 m resolution for shallow water propagation and runup computation. Even though using a realistic, high-resolution nearshore bathymetry will change the details of the results (i.e. modelled tsunami runup values in Fig. 5b), our simplified coarse bathymetric model is sufficient for the purpose of the numerical experiment described above. We assumed an open radiation boundary condition to the outer sea and a moving boundary on the coast. The computation time step for all grids was set to satisfy the Courant–Friedrichs–Lewy stability condition of the finite difference method. All tsunami simulations were run for 1 h, which we checked was long enough to obtain the largest runup at the coast (in this case associated with the leading wave).

## Data availability

Diatom, sedimentology, stratigraphy and radiocarbon data sets are available on the Figshare repository with the identifier: <https://doi.org/10.6084/m9.figshare.16617241>. Data sets used for tsunami modelling are freely available online or from linked references in the “Methods” section (COMCOT tsunami code and dislocation model<sup>53</sup>; SLAB geometry<sup>52</sup>; GEBCO bathymetry from [www.gebco.net](http://www.gebco.net)). LiDAR data were donated by Forestal Arauco to the CYCLO project under a confidentiality agreement and may be obtained from the corresponding author upon reasonable request.

## Code availability

The COMCOT tsunami code is available from Wang<sup>53</sup> and the dislocation modelling code as described in Gao et al.<sup>51</sup> was provided by Kelin Wang. No new computer code was written in preparing the paper.

Received: 16 February 2021; Accepted: 4 November 2021;

Published online: 09 December 2021

## References

- Jankaew, K. et al. Medieval forewarning of the 2004 Indian Ocean tsunami in Thailand. *Nature* **455**, 1228–1231 (2008).
- Stein, S. & Okal, E. A. The size of the 2011 Tohoku earthquake need not have been a surprise. *Eos* **92**, 227–228 (2011).
- Geller, R. J. Shake-up time for Japanese seismology. *Nature* **472**, 407–409 (2011).
- Cisternas, M., Torrejón, F. & Gorigoitia, N. Amending and complicating Chile's seismic catalog with the Santiago earthquake of 7 August 1580. *J. South American Earth Sci.* **33**, 102–109 (2012).
- Ishibashi, K. Status of historical seismology in Japan. *Ann. Geophys.* **47**, 339–368 (2004).
- Garrett, E. et al. A systematic review of geological evidence for Holocene earthquakes and tsunamis along the Nankai-Suruga Trough, Japan. *Earth Sci. Rev.* **159**, 337–357 (2016).
- Dura, T. et al. Subduction zone slip variability during the last millennium, south-central Chile. *Quaternary Sci. Rev.* **175**, 112–137 (2017).
- Ely, L. L., Cisternas, M., Wesson, R. L. & Dura, T. Five centuries of tsunamis and land-level changes in the overlapping rupture area of the 1960 and 2010 Chilean earthquakes. *Geology* **42**, 995–998 (2014).
- Cisternas, M. et al. Predecessors of the giant 1960 Chile earthquake. *Nature* **437**, 404–407 (2005).
- Cisternas, M., Garrett, E., Wesson, R., Dura, T. & Ely, L. L. Unusual geologic evidence of coeval seismic shaking and tsunamis shows variability in earthquake size and recurrence in the area of the giant 1960 Chile earthquake. *Mar. Geol.* **385**, 101–113 (2017).
- Garrett, E. et al. Reconstructing paleoseismic deformation, 2: 1000 years of great earthquakes at Chucalen, south central Chile. *Quaternary Sci. Rev.* **113**, 112–122 (2015).
- Kemp, P. et al. Coastal lake sediments reveal 5500 years of tsunami history in south central Chile. *Quaternary Sci. Rev.* **161**, 99–116 (2017).
- Moernaut, J. et al. Giant earthquakes in South-Central Chile revealed by Holocene mass-wasting events in Lake Puyehue. *Sediment. Geol.* **195**, 239–256 (2007).
- Moernaut, J. et al. Lacustrine turbidites as a tool for quantitative earthquake reconstruction: new evidence for a variable rupture mode in south central Chile. *J. Geophys. Res. Solid Earth* **119**, 1607–1633 (2014).
- St-Onge, G. et al. Comparison of earthquake-triggered turbidites from the Saguenay (Eastern Canada) and Reloncavi (Chilean margin) Fjords: implications for paleoseismicity and sedimentology. *Sediment. Geol.* **243**, 89–107 (2012).
- Cisternas, M., Carvajal, M., Wesson, R., Ely, L. L. & Gorigoitia, N. Exploring the historical earthquakes preceding the giant 1960 Chile earthquake in a time-dependent seismogenic zone. *Bull. Seismol. Soc. Am.* **107**, 2664–2675 (2017).
- Nentwig, V. et al. Multiproxy analysis of tsunami deposits - the Tirúa example, central Chile. *Geosphere* **14**, 1067–1086 (2018).
- Nentwig, V., Tsukamoto, S., Frechen, M. & Bahlburg, H. Reconstructing the tsunami record in Tirúa, Central Chile beyond the historical record with quartz-based SAR-OSL. *Quaternary Geochronol.* **30**, 299–305 (2015).
- Plafker, G. & Savage, J. C. Mechanism of the Chilean earthquakes of May 21 and 22, 1960. *Geol. Soc. Am. Bull.* **81**, 1001–1030 (1970).
- Hocking, E. P., Garrett, E. & Cisternas, M. Modern diatom assemblages from Chilean tidal marshes and their application for quantifying deformation during past great earthquakes. *J. Quaternary Sci.* **32**, 396–415 (2017).
- Hua, Q. Radiocarbon: a chronological tool for the recent past. *Quaternary Geochronol.* **4**, 378–390 (2009).
- Aedo, D., Melnick, D., Garrett, E. & Pino, M. Source and distribution of tsunami deposits at Chaihuín marsh (40°S/73.5°W), Chile. *Andean Geol.* **48**, 125–152 (2021).
- Sawai, Y. et al. Diatom assemblages in tsunami deposits associated with the 2004 Indian Ocean tsunami at Phra Thong Island, Thailand. *Mar. Micropaleontol.* **73**, 70–79 (2009).
- Hong, I. et al. A 600-year-long stratigraphic record of tsunamis in south-central Chile. *Holocene* **27**, 39–51 (2017).
- Dura, T. et al. Coastal evidence for Holocene subduction-zone earthquakes and tsunamis in central Chile. *Quaternary Sci. Rev.* **113**, 93–111 (2015).
- Tanigawa, K., Sawai, Y. & Namegaya, Y. Diatom assemblages within tsunami deposit from the 2011 Tohoku-oki earthquake along the Misawa coast, Aomori Prefecture, northern Japan. *Mar. Geol.* **396**, 6–15 (2018).
- Witter, R. C., Kelsey, H. M. & Hemphill-Haley, E. Great Cascadia earthquakes and tsunamis of the past 6700 years, Coquille River estuary, southern coastal Oregon. *Geol. Soc. Am. Bull.* **115**, 1289–1306 (2003).
- Matsumoto, D. et al. Erosion and sedimentation during the September 2015 flooding of the Kinu River, central Japan. *Sci. Rep.* **6**, 34168 (2016).
- Witter, R. C., Kelsey, H. M. & Hemphill-Haley, E. Pacific storms, El Niño and tsunamis: competing mechanisms for sand deposition in a coastal marsh, Euchre Creek, Oregon. *J. Coast. Res.* **17**, 563–583 (2001).
- Shennan, I., Garrett, E. & Barlow, N. Detection limits of tidal-wetland sequences to identify variable rupture modes of megathrust earthquakes. *Quaternary Sci. Rev.* **150**, 1–30 (2016).
- Nelson, A. R., Shennan, I. & Long, A. J. Identifying coseismic subsidence in tidal-wetland stratigraphic sequences at the Cascadia subduction zone of western North America. *J. Geophys. Res.* **101**, 6115–6135 (1996).
- Udías, A., Madariaga, R., Buforn, E., Muñoz, D. & Ros, M. The large Chilean historical earthquakes of 1647, 1657, 1730, and 1751 from contemporary documents. *Bull. Seismol. Soc. Am.* **102**, 1639–1653 (2012).
- Carvajal, M. et al. Reexamination of the magnitudes for the 1906 and 1922 Chilean earthquakes using Japanese tsunami amplitudes: Implications for source depth constraints. *J. Geophys. Res. Solid Earth* **122**, 4–17 (2017).
- Okada, Y. Surface deformation due to shear and tensile faults in a half-space. *Bull. Seismol. Soc. Am.* **75**, 1135–1154 (1985).
- Barlow, N. L. M. et al. Salt marshes as late Holocene tide gauges. *Glob. Planet. Chang.* **106**, 90–110 (2013).
- Hamilton, S. & Shennan, I. Late Holocene relative sea-level changes and the earthquake deformation cycle around upper Cook Inlet, Alaska. *Quaternary Sci. Rev.* **24**, 1479–1498 (2005).
- Shennan, I. et al. Tidal marsh stratigraphy, sea-level change and large earthquakes, I: a 5000 year record in Washington, USA. *Quaternary Sci. Rev.* **15**, 1023–1059 (1996).

38. Dura, T., Hemphill-Haley, E., Sawai, Y. & Horton, B. P. The application of diatoms to reconstruct the history of subduction zone earthquakes and tsunamis. *Earth Sci. Rev.* **152**, 181–197 (2016).
39. Engel, M., Pilarczyk, J., May, S. M., Brill, D. & Garrett, E. *Geological Records of Tsunamis and Other Extreme Waves* (Elsevier, 2020).
40. Dura, T. & Hemphill-Haley, E. in *Geological Records of Tsunamis and Other Extreme Waves* (eds Engel, M. et al.) Ch. 14 (Elsevier, 2020).
41. Gibbs, R. J., Matthews, M. D. & Link, D. A. Relationship between sphere size and settling velocity. *J. Sediment. Petrol.* **41**, 7–18 (1971).
42. Balsillie, J. H., Donoghue, J. F., Butler, K. M. & Koch, J. L. Plotting equation for Gaussian percentiles and a spreadsheet program for generating probability plots. *J. Sediment. Res.* **72**, 929–933 (2002).
43. Schindelin, J. et al. Fiji: an open-source platform for biological-image analysis. *Nat. Methods* **9**, 676–682 (2012).
44. Watcham, E. P., Shennan, I. & Barlow, N. L. M. Scale considerations in using diatoms as indicators of sea-level change: lessons from Alaska. *J. Quaternary Sci.* **28**, 165–179 (2013).
45. Sawai, Y. et al. Relationships between diatoms and tidal environments in Oregon and Washington, USA. *Diatom Res.* **31**, 17–38 (2016).
46. Gehrels, W. R., Roe, H. M. & Charman, D. J. Foraminifera, testate amoebae and diatoms as sea-level indicators in UK saltmarshes: a quantitative multiproxy approach. *J. Quaternary Sci.* **16**, 201–220 (2001).
47. Marshall, W. A. et al. The use of ‘bomb spike’ calibration and high-precision AMS C-14 analyses to date salt-marsh sediments deposited during the past three centuries. *Quaternary Res.* **68**, 325–337 (2007).
48. Hogg, A. G. et al. SHCal20 Southern Hemisphere calibration 0–55,000 years cal BP. *Radiocarbon* **62**, 759–778 (2020).
49. Hua, Q. & Barbetti, M. Review of tropospheric bomb C-14 data for carbon cycle modeling and age calibration purposes. *Radiocarbon* **46**, 1273–1298 (2004).
50. Bronk Ramsey, C. Bayesian analysis of radiocarbon dates. *Radiocarbon* **51**, 337–360 (2009).
51. Gao, D. et al. Defining megathrust tsunami source scenarios for northernmost Cascadia. *Natural Hazards* **94**, 445–469 (2018).
52. Tassara, A. & Echaurren, A. Anatomy of the Andean subduction zone: three-dimensional density model upgraded and compared against global-scale models. *Geophys. J. Int.* **189**, 161–168 (2012).
53. Wang, X. *User Manual for COMCOT Version 1.7 (First Draft)* (Cornell University, 2009).
54. Melnick, D., Bookhagen, B., Strecker, M. R. & Echtler, H. P. Segmentation of megathrust rupture zones from fore-arc deformation patterns over hundreds to millions of years, Arauco peninsula, Chile. *J. Geophys. Res. Solid Earth* **114**, B01407 (2009).
55. Angermann, D., Klotz, J. & Reigber, C. Space-geodetic estimation of the Nazca-South America Euler vector. *Earth Planet. Sci. Lett.* **171**, 329–334 (1999).

## Acknowledgements

This research was funded by the Natural Environment Research Council (New Investigator Award NE/K000446/1), the European Union/Durham University (COFUND under the DIFeREns 2 scheme), the Millennium Scientific Initiative (ICM) of the Chilean Government (Grant Number NC160025 “Millennium Nucleus CYCLO: The Seismic Cycle Along Subduction Zones”), Chilean National Fund for Development of Science and Technology (FONDECYT grants 1190258 and 1181479) and the ANID PIA Anillo

ACT192169. Radiocarbon dating support was provided by the Natural Environment Research Council Radiocarbon Facility (1707.0413, 1795.0414 and 2000.0416). LiDAR data were provided by Forestal Arauco under a collaboration agreement. We gratefully acknowledge Steve Moreton for providing the radiocarbon dates from NERC-RCF, Kelvin Wang for providing the dislocation model used herein and Neil Tunstall and Chris Longley for help with core scanning. We thank Francisco Villagrán, Carlos Torres, Bill Austin, Martin Brader and Joaquim Otero for help in the field and the staff of the Valdivian coastal reserve for the facilities they provided. All sampling was undertaken with consent from the landowners; permission was acquired verbally. We thank Marco Cisternas for his insights into coastal palaeoseismology and three anonymous reviewers for their constructive comments to improve the paper. This paper forms a contribution to IGCP Projects 639 and 725.

## Author contributions

E.G., D.M., D.A. and E.P.H. conducted fieldwork; E.P.H. and E.G. conducted diatom analyses, developed the transfer function and developed the age model; D.A. led the sedimentological analysis; M.C. and D.M. performed the rupture and tsunami modelling; E.P.H. wrote the paper with input from all authors.

## Competing interests

The authors declare no competing interests.

## Additional information

**Supplementary information** The online version contains supplementary material available at <https://doi.org/10.1038/s43247-021-00319-z>.

**Correspondence** and requests for materials should be addressed to Emma P. Hocking.

**Peer review information** *Communications Earth & Environment* thanks SeanPaul La Selle and the other anonymous reviewer(s) for their contribution to the peer review of this work. Primary handling editors: Adam Switzer, Joe Aslin. Peer reviewer reports are available.

**Reprints and permission information** is available at <http://www.nature.com/reprints>

**Publisher’s note** Springer Nature remains neutral with regard to jurisdictional claims in published maps and institutional affiliations.



**Open Access** This article is licensed under a Creative Commons Attribution 4.0 International License, which permits use, sharing, adaptation, distribution and reproduction in any medium or format, as long as you give appropriate credit to the original author(s) and the source, provide a link to the Creative Commons license, and indicate if changes were made. The images or other third party material in this article are included in the article’s Creative Commons license, unless indicated otherwise in a credit line to the material. If material is not included in the article’s Creative Commons license and your intended use is not permitted by statutory regulation or exceeds the permitted use, you will need to obtain permission directly from the copyright holder. To view a copy of this license, visit <http://creativecommons.org/licenses/by/4.0/>.

© The Author(s) 2021